



Z-scheme $\text{BiO}_{1-x}\text{Br}/\text{Bi}_2\text{O}_2\text{CO}_3$ photocatalyst with rich oxygen vacancy as electron mediator for highly efficient degradation of antibiotics

Jie Ding, Zan Dai, Fan Qin, Huiping Zhao, Shuai Zhao, Rong Chen*

Key Laboratory for Green Chemical Process of Ministry of Education and School of Chemistry and Environmental Engineering, Wuhan Institute of Technology, Xiongchu Avenue, Wuhan, 430073, PR China

ARTICLE INFO

Article history:

Received 19 September 2016

Received in revised form 28 October 2016

Accepted 7 December 2016

Available online 8 December 2016

Keywords:

Oxygen vacancies

$\text{BiO}_{1-x}\text{Br}/\text{Bi}_2\text{O}_2\text{CO}_3$

Z-scheme

Electron mediator

Antibiotics

ABSTRACT

To solve serious energy and environmental crises caused by rapid industrial development, Z-scheme photocatalytic system provides a potential strategy to as ideal photocatalyst with wide absorption range, high charge-separation efficiency and strong redox ability. In this work, we develop a facile time-dependent method to fabricate Z-scheme $\text{BiO}_{1-x}\text{Br}/\text{Bi}_2\text{O}_2\text{CO}_3$ photocatalyst with rich oxygen vacancies for visible light photocatalysis, which exhibits highly enhanced performance for antibiotics (CIP, 4-MAA etc.) photodegradation. A possible mechanism of the improved photocatalytic efficiency based on the Z-scheme photocatalytic system formed via oxygen vacancy is also proposed. Oxygen vacancies, acting as electron mediator, could significantly promote the separation of photoinduced charge carriers. Due to the increase of redox ability, it benefits to the production of superoxide radical ($\bullet\text{O}_2^-$) on the CB of $\text{BiO}_{1-x}\text{Br}$ and hydroxyl radical ($\bullet\text{OH}$) on the VB of $\text{Bi}_2\text{O}_2\text{CO}_3$, respectively. This work demonstrates that a simple oxygen vacancy involved Z-scheme photocatalytic system could efficiently enhance the photocatalytic activity for the degradation of pollutants.

© 2016 Elsevier B.V. All rights reserved.

1. Introduction

Widely used antibiotics in the natural environment raise several big concerns over their negative impacts on ecosystem and human health [1]. The residual antibiotics in the environment could result in various adverse effects and hinder the wastewater treatment [2]. For example, continuous release of antibiotics into aquatic environment could promote bacterial resistance [3,4]. Furthermore, formed stable organic byproducts during antibiotics treatment is difficult to further degrade and could cause secondary pollution, as well as lead to antibiotics resistance in bacterial populations [4–6]. Therefore, it is urgently essential to develop an efficient organic carbon mineralization process for antibiotics removal in water treatment.

Undoubtedly, photocatalysis is an ideal light-driven chemical process for the antibiotics degradation, which is an economical and environmental-friendly technology in wastewater treatment [7,8]. In order to realize the organic carbon mineralization of residual antibiotics in wastewater, it requires suitable band gap of photocatalyst to harvest the solar energy in visible region, as well as appropriate band edge positions, i.e. the redox potential of antibi-

otic should be located between the bottom of the conduction band (CB) and the top of the valence band (VB) of the photocatalyst [9,10]. However, single component photocatalyst cannot be characterized with both wide light-absorption range and strong redox ability, simultaneously. Even though, heterostructure photocatalytic materials could improve the photocatalytic ability by providing good visible-light response and efficient electron-hole pair separation, the decline of oxidability and reducibility still limits their practical application [11–14]. Recently, it is found that Z-scheme is an effective strategy to improve the photocatalytic performance of heterojunction photocatalyst [8,15–20]. Properly designed Z-scheme photocatalytic system could realize the balance of photon number between the two semiconductors by utilizing two photons generating an electron-hole pair, while the other electron-hole pair recombines at the interface of semiconductors. At the same time, Z-scheme photocatalytic system remains high reduction and oxidation ability at two different reaction sites. For examples, N. Srinivasan et al. developed a bulk heterojunction Z-scheme system consisting of *p*-type CaFe_2O_4 and *n*-type BiVO_4 semiconductors for overall water splitting [21]. R. Amal et al. demonstrated that reduced graphene oxide could work as a solid-state electron mediator in Z-scheme photocatalytic water splitting under visible light [10]. It was found that the appropriate shuttle redox mediator played a significant role in the Z-scheme photocatalytic system,

* Corresponding author.

E-mail address: rchenhku@hotmail.com (R. Chen).



Table 1The detailed experimental parameters^a.

Samples	Molar ratio of NaBr/Bi(NO ₃) ₃	Reaction time (h)
BRC-1	0.5	6
BRC-2	0.5	3
BRC-3	1	6
BRC-4	1	3
BRC-5	0	6

^a The amount of Bi(NO₃)₃ is 1 mmol, reaction temperature is 180 °C and the solvent is mannitol aqueous solution (25 mL, 0.1 M).

which acted as electron conductor for the electron transfer from the CB of oxidation system to the VB of the reduction system.

In this work, we developed a facile solvothermal method to construct BiO_{1-x}Br/Bi₂O₂CO₃ Z-scheme system by varying the content of NaBr and reaction time. The photodegradation of antibiotics over Z-scheme BiO_{1-x}Br/Bi₂O₂CO₃ heterojunction has been studied under visible light irradiation. To understand the significantly enhanced visible-light-driven photocatalytic ability of the Z-scheme BiO_{1-x}Br/Bi₂O₂CO₃ system, the band structures, optical and electrochemical properties, separation and transfer of photogenerated electron-hole pairs, and the generation of reactive species of the Z-scheme BiO_{1-x}Br/Bi₂O₂CO₃ heterojunction during photocatalytic process were investigated. It was found that the oxygen vacancy in BiO_{1-x}Br/Bi₂O₂CO₃ heterojunction acted as electron mediator in Z-Scheme photocatalytic system, which was seldom reported. A possible degradation mechanism of the improved photocatalytic performance was also proposed. This work provides an effective strategy for the fabrication of Z-scheme photocatalytic system to improve its photocatalytic ability.

2. Experimental section

2.1. Materials

Bismuth nitrate pentahydrate (Bi(NO₃)₃·5H₂O), 4-methylaminoantipyrine (4-MAA), bisphenol-A (BPA) were purchased from Aladdin (Shanghai, China). Manitol, sodium bromide (NaBr), ciprofloxacin (CIP), sodium sulfate (Na₂SO₄), ter-butyl alcohol (TBA), terephthalic acid (TA), and nitrobluetetrazolium (NBT) were purchased from Sinopharm Chemical Reagent Co., Ltd. (Shanghai, China). All the reagents were analytical grade and used directly without further purification.

2.2. Synthesis

In a typical synthesis, 0.485 g (1 mmol) of Bi(NO₃)₃·5H₂O and 0.0515 g (0.5 mmol) NaBr were dissolved into 25 mL mannitol aqueous solution (0.1 M), respectively. Then the obtained transparent solution was transferred to a Teflon-lined stainless steel autoclave to perform solvothermal process at 180 °C for 6 h. After cooling down to room temperature naturally, the solid product was collected by centrifugation and washed with deionized water and ethanol for five times. The sample was finally dried in a vacuum oven for 24 h at 60 °C for further characterization (BRC-1). Other samples were also prepared under identical conditions by varying the amount of NaBr and reaction time. The detailed experimental parameters are listed in Table 1.

2.3. Characterization

Powder X-ray diffraction (XRD) was carried out on Bruker axs D8 Discover (Cu K=1.5406 Å) at a scan rate of 2° min⁻¹ in the 2θ range from 10–80°. Scanning electron microscopy (SEM) images were performed on Hitachi S4800 scanning electron microscope with 5.0 kv. Transmission electron microscope (TEM) image were

performed on JEOL JSM-2010, transmission electron microscope with 200 kV. X-ray photoelectron spectra (XPS) were performed on a VG Multilab2000 spectrometer by using Al K α (1486.6 eV) radiation as the source. All the binding energy (BE) values were calibrated by the C 1s peak at 284.6 eV of the surface adventitious carbon. The electron spin resonance (ESR) measurement were carried out by using a Bruker EMX 10/2.7 ESR spectrometer (X-band) equipped dual cavity with modulation and microwave frequencies of 100 kHz and 9.4145 GHz, respectively. The g-factors were determined by the WinEPR program. Temperature-programmed oxidation (TPO) experiments were performed from room temperature to 350 °C with heating rate of 5 °C min⁻¹ under O₂ (5%)/He flow. UV-vis diffuse reflectance spectra (DRS) were recorded on a UV-vis spectrometer (Hitachi UH4150) and were converted from reflection to absorbance by the Kubelka-Munk method. Photoluminescence spectra (PL) were detected with a Hitachi F4600 fluorescence spectrophotometer. Brunauer-Emmett-Teller (BET) specific surface area of the powders was analyzed by nitrogen adsorption in a Micromeritics ASAP 2020 nitrogen adsorption apparatus (USA). All the as-prepared samples were degassed at 150 °C for 4 h prior to nitrogen adsorption measurements.

2.4. Photocatalytic activity evaluation

Photocatalytic activities of the samples were evaluated by the photocatalytic degradation of CIP (40 mg/L), BPA (20 mg/L) and 4-MAA (50 mg/L) under visible light irradiation by using a 500 W Xe lamp (10 mW/cm², measured by EL-NP2000, Beijing China Education Au-light Co. Ltd) with a 420 nm cutoff filter (Bilon Co. Ltd, Shanghai, China). In a typical photocatalytic experiment, 0.01 g photocatalyst was dispersed in CIP (or BPA, or 4-MAA) solution (40 mL) in a cylindrical vessel. The suspension was stirred in dark for 2 h to ensure an adsorption-desorption equilibrium before irradiation. Then, the suspension was exposed to visible light irradiation. At each given time interval, 3 mL suspension was sampled and centrifuged to remove the solid photocatalyst. The concentration of pollutant during the degradation were monitored by colorimetry using a Shimadzu UV2800 spectrophotometer. All photocatalytic reactions were carried out at room temperature.

2.5. Analysis of intermediates and final products in photocatalysis

The intermediates during photocatalysis was analyzed by high-performance liquid chromatography-mass spectrometry (HPLC/MS) technique (Agilent 1260/6310, Ion Trap LC/MS) equipped with a Poroshell 120 SB-C18 column (150 mm × 4.6 mm i.d., 2.7 μm). The mobile phase composed of water (65%) and acetonitrile (35%, containing 0.2% formic acid) for CIP, water (45%, 25%) and methanol (55%, 75%) for BPA and 4-MAA, respectively. And the flow rate was 0.2 mL/min. The gradient started with 20% acetonitrile or methanol, increased to 30% within 2.5 min and to 80% within 3.5 min and then returned to the initial composition within 5 min and equilibrated within 4 min. The injection volume was 20 μL, and the column temperature was 30 °C. MS was performed by operating in the negative ion mode using ESI under the following conditions: capillary, 27 nA; nebulization pressure, 30 psi; temperature of drying gas, 300 °C; drying gas flow, 10 L/min. MS was scanned in a *m/z* range from 100 to 800. Organic carbon mineralization was determined by total organic carbon (TOC) analysis, performed on a Dohrmann Phoenix 8000 UV-persulfate TOC analyzer.

2.6. Determination of reactive species

To detect the generation of active species, ESR signals of radicals spin-trapped by 5,5-dimethyl-L-pyrroline-N-oxide (DMPO) were collected on a Bruker EMX-8/2.7 X-band EPR spectrometer under

visible light illumination ($\lambda > 400$ nm). DMPO-•O₂⁻ and DMPO-•OH spins trapping ESR spectra were collected in methanol solution and aqueous solution under visible light irradiation for 20 min in the presence of the corresponding photocatalyst. The relative concentration of •OH was estimated by a TA fluorescence method. The fluorescence test was conducted by dissolving TA in 2.0 mM NaOH. Then, 0.1 g of the photocatalyst was added to 100 mL of the solution, and the mixture was irradiated under visible light and measured on a Hitachi F-4600 fluorescence spectrophotometer with an excitation wavelength of 315 nm. NBT was used to determine the generation of •O₂⁻ in the photocatalytic process. 0.10 g photocatalyst was dispersed in 100 mL of the NBT aqueous solution (2.5×10^{-5} mol/L). Then, the suspension was irradiated under visible light and 5 mL of sample was measured on Evolution 220 UV-vis spectrophotometer every 40 min *tert*-butyl alcohol (t-BuOH, 10 mM) and Nitrogen gas (N₂) was used as •OH and •O₂⁻ scavenger in the photocatalysis, respectively.

2.7. Photoelectrochemical experiments

The photocurrent measurement, electrochemical impedance spectroscopy (EIS) measurement, and Mott-Schottky experiment were carried out on a CHI 660E workstation (Shanghai, China) in a standard three-electrode cell, which contained 0.5 M Na₂SO₄ aqueous solution with a platinum foil and a saturated calomel electrode as the counter electrode and the reference electrode, respectively. The working electrode was prepared according to the following process: 10 mg as-prepared sample was mixed with 0.4 mL DMF and 0.1 mL nafion solution (5%, DuPont) to form homogeneous emulsion. Then 0.2 mL the catalyst emulsion was dropwise coated on a 10 mm × 10 mm indium-tin oxide (ITO) glass electrode. The estimated loading amount of the sample is 1 mg/cm². After drying in room temperature, the as-prepared electrode was further annealed at 150 °C for 4 h in a vacuum oven to remove the resin. Photocurrent responses of the photocatalyst were measured at open-circuit potential upon light on and off, with simulated light irradiation provided by a 500 W Xe lamp. Electrochemical impedance spectroscopy (EIS) and Mott-Schottky curve were carried out at the open-circuit potential in 0.5 M potassium ferricyanide solution. Samples were dip coated into a glassy carbon working electrode. A sinusoidal AC perturbation of 5 mV was applied to the electrode over the frequency range 0.5–10⁵ Hz. A glassy carbon disk was used as the working electrode with a diameter of 3 mm, a Pt foil auxiliary electrode as the counter electrode and an Ag/0.01 M AgNO₃ with 0.1 M tetrabutylammonium hexafluorophosphate (TBAPF₆) acetonitrile as reference electrode completed the three electrode set-up.

3. Results and discussion

3.1. Composition and morphology

Fig. 1 shows the XRD patterns of the products prepared under different conditions. It reveals that the products obtained in the absence of NaBr (**BRC-5**) and in the presence of 1 mmol NaBr (**BRC-3** and **BRC-4**) could be well indexed to orthorhombic Bi₂O₂CO₃ (JCPDS 84-1752) and cubic phase BiOBr (JCPDS 73-2061), respectively. It illustrates that pure BiOBr and Bi₂O₂CO₃ could be prepared under the corresponding conditions. However, when the molar ratio of NaBr/Bi(NO₃)₃ was changed to 0.5 (**BRC-1** and **BRC-2**), the characteristic diffraction peaks of the samples could be assigned to two different phases, which was corresponding to cubic phase BiOBr (JCPDS 73-2061) and orthorhombic Bi₂O₂CO₃ (JCPDS 84-1752), respectively. No additional impurity phase was found in this diffraction pattern, indicative of the formation of

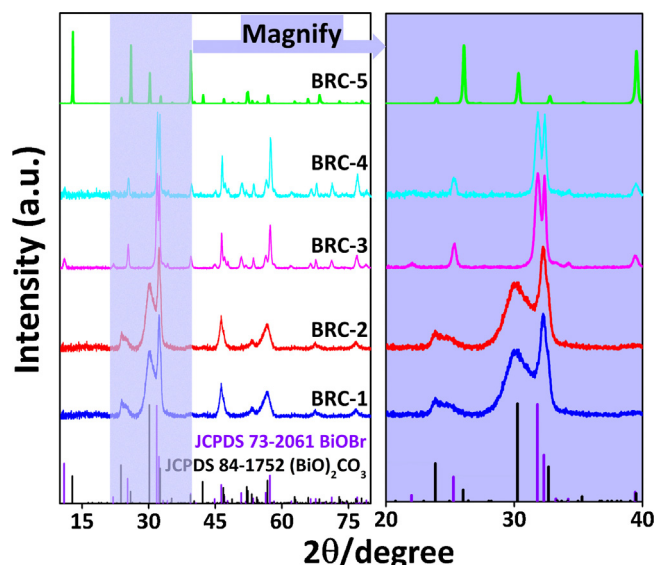


Fig. 1. XRD patterns of **BRC** samples prepared under different conditions.

BiOBr/Bi₂O₂CO₃ composites. SEM images demonstrate the aggregated nanoplate-like morphology of the obtained samples (Fig. S1, Supporting Information). The results illustrate that BiOBr/Bi₂O₂O₃ nanocomposites could be fabricated by varying the molar ratio of NaBr/Bi(NO₃)₃. Interestingly, no difference in composition and morphology was observed for BiOBr/Bi₂O₂CO₃ nanocomposites obtained at different hydrothermal reaction time (**BRC-1** and **BRC-2**). Similar XRD pattern and morphology was also observed in single component BiOBr samples obtained at different reaction time.

3.2. Photodegradation efficiency and products

However, the samples with same composition and morphology exhibit completely different photocatalytic performance for the degradation of antibiotics. The photocatalytic activities of **BRC** samples were evaluated by the photodecomposition of colorless CIP under visible light illumination. Fig. 2a shows the variation of CIP concentration (C_t/C_0) with irradiation time over different **BRC** samples. Among the tested samples, BiOBr/Bi₂O₂CO₃ nanocomposite obtained after 6 h of hydrothermal treatment (**BRC-1**) exhibits the highest photocatalytic activity for CIP photodegradation, which is much higher than that of BiOBr/Bi₂O₂CO₃ nanocomposite obtained after 3 h of hydrothermal treatment (**BRC-2**). For comparison, the direct photolysis of CIP in the absence of photocatalyst demonstrates no obvious variation of CIP concentration upon visible light irradiation. It is worth noticed that the mixture of **BRC-3** and **BRC-5** also displays much poor photodegradation efficiency than that of **BRC-1**. It further confirms the formation of BiOBr/Bi₂O₂CO₃ heterostructure nanocomposites, which could improve the photocatalytic performance. In addition, the kinetics data of CIP photodegradation reaction over **BRC** samples fit to a pseudo-first-order model, which is expressed as [22,23]:

$$\ln(C_0/C_t) = kt \quad (1)$$

where C_0 and C_t represents the concentration of CIP before and after irradiation, t is irradiation time and k is the apparent rate constant, as shown in Fig. S2 (Supporting Information). To exclude the effect of BET surface area (Fig. S3, Supporting Information), the values of apparent rate constant per unit surface area of the catalysts (k/S_{BET}) are calculated determined to evaluate the photocatalytic efficiency of **BRC** samples (Fig. 2b). **BRC-1** also possesses the highest k/S_{BET} value of $15.51 \times 10^{-3} \text{ m}^{-2} \cdot \text{H}^{-1}$ among the samples, which benefits the improvement of photocatalytic efficiency [24].

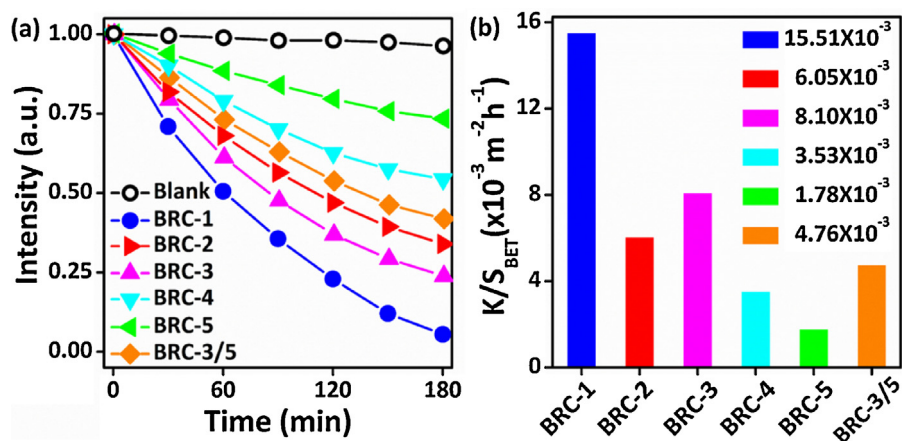


Fig. 2. Photodegradation efficiency of CIP (a) and pseudo-first-order kinetic constants per unit surface area (b) of BRC samples under visible light irradiation.

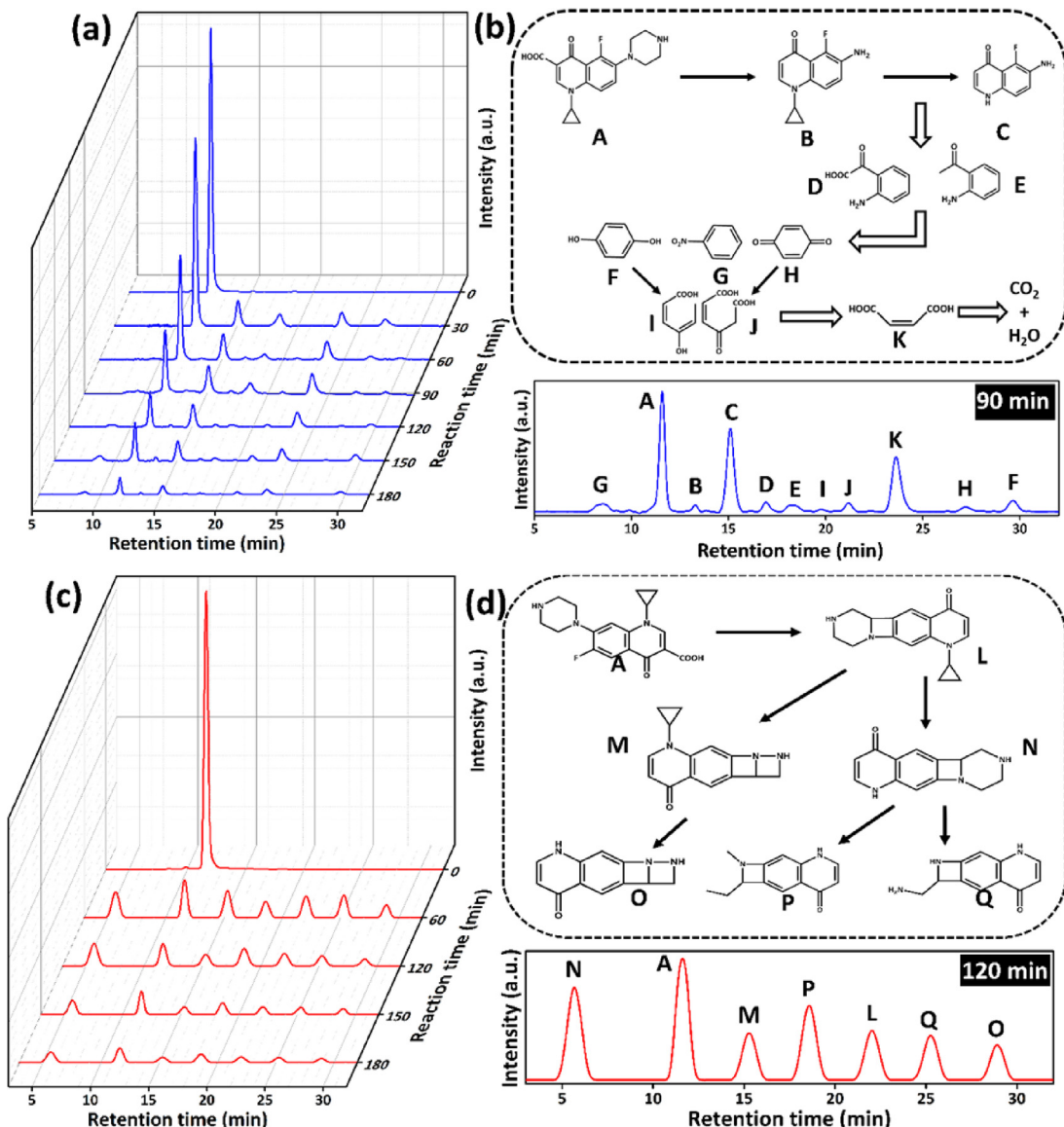


Fig. 3. Representative HPLC chromatograms (a, c) and the proposed degradation pathway (b, d) of CIP photodegradation over BRC-1 (a, b) and BRC-2 (c, d) upon visible-light irradiation.

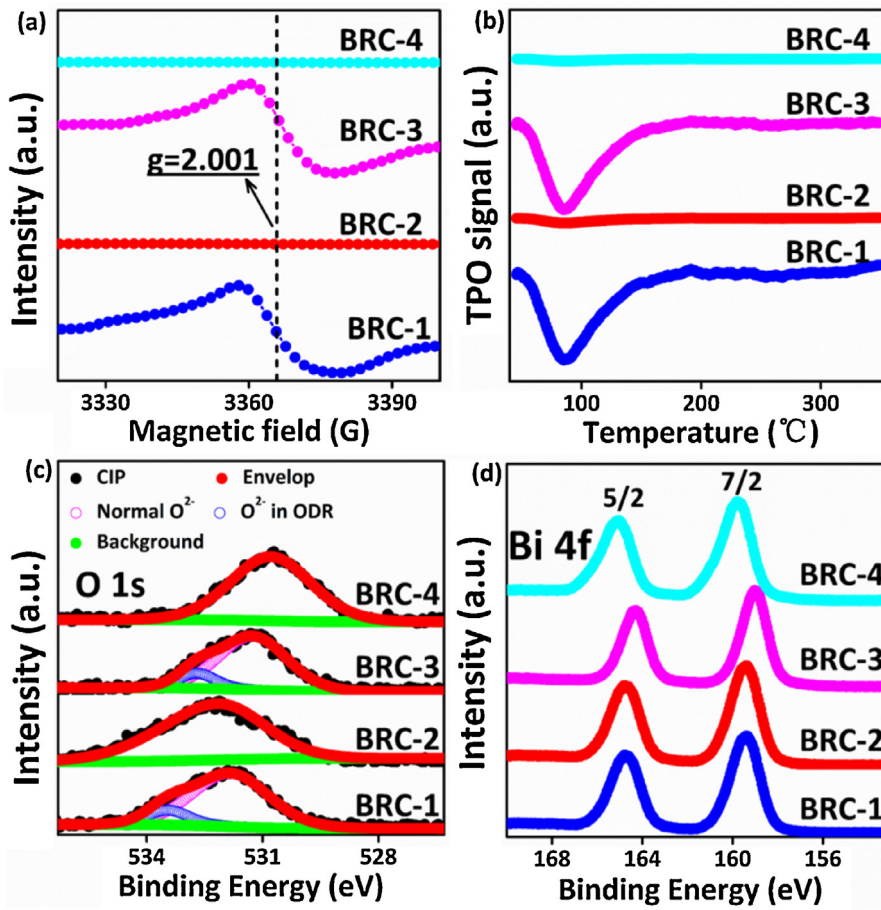


Fig. 4. ESR spectra (a), TPO profile (b), and High-resolution O 1s (c), and Bi 4f (d) XPS spectra of **BRC** samples.

More importantly, the different photocatalytic abilities of the BiOBr/Bi₂O₂CO₃ nanocomposites are also reflected in the degradation pathway and final products of CIP. Fig. 3 shows the HPLC-MS analysis of CIP photodegradation over **BRC-1** and **BRC-2**. As shown in Fig. 3a and c, the peak intensity of CIP decreases gradually with the increase of irradiation time. However, the corresponding mass spectra of the intermediates reveal the different degradation pathway and final products of CIP over **BRC-1** and **BRC-2** (Fig. S4, Supporting Information). On the basis of the identified intermediates and the reported literature [25,26], the possible photodegradation pathway of CIP over **BRC-1** and **BRC-2** is proposed, as summarized in Fig. 3b and 3d. It was found that CIP could be completely degraded to carbon dioxide and water over **BRC-1** within 3 h. However, the full analysis of HPLC-MS spectra of CIP photodegradation over **BRC-2** demonstrates that the quinolone moiety is hardly degraded (Fig. 3d). In addition, the TOC removal (%) is calculated to evaluate the mineralization of organic contaminates. As shown in Fig. S5 (Supporting Information), CIP could be completely mineralized in the presence of **BRC-1**. Unfortunately, the presence of **BRC-2** cannot effectively mineralize CIP, and TOC removal (%) is only about 50% after 3 h photodegradation reaction. It illustrates that BiOBr/Bi₂O₂CO₃ nanocomposites with identical crystal phase, composition, morphology and BET surface area displayed significantly different photocatalytic performance for antibiotics degradation. Moreover, the same phenomena was also observed in single component BiOBr photocatalyst. **BRC-3** exhibits much higher photocatalytic efficiency than that of **BRC-4**, which possesses the similar crystal phase, morphology and BET surface area with **BRC-3**. Most importantly, single-component **BRC-3** displays higher pho-

tocatalytic activity than that of heterostructured BiOBr/Bi₂O₂CO₃ nanocomposites (**BRC-2**).

3.3. Oxygen vacancy determination

In order to elucidate the reason of different photocatalytic activity over the samples with same composition, the ESR spectra of the **BRC** samples obtained under different reaction conditions are performed. As shown in Fig. 4a, the intensified ESR signals at 3357 G (with g value of 2.001) are observed in the ESR spectra of **BRC-1** and **BRC-3**, which is attributed to the Zeeman Effect of single electron trapped by oxygen vacancies [27,28]. On the contrary, no signal is detected in the ESR spectra of **BRC-2** and **BRC-4**. It demonstrates that oxygen vacancies could be generated after prolonging the reaction, regardless of whether in BiOBr sample or BiOBr/Bi₂O₂CO₃ nanocomposites. To further confirm the content of produced oxygen vacancies, we also performed TPO analysis of the **BRC** samples. Fig. 4b shows the TPO profiles obtained from different **BRC** samples. Only **BRC-1** and **BRC-3** shows one peak centered at 90 °C, which could be attributed to the oxidation of cation vacancies [29]. And the peak of **BRC-1** and **BRC-3** displays similar peak shape and area, indicative of same oxygen vacancy concentration in **BRC-1** and **BRC-3**. However, no TPO signal is detected in **BRC-2** and **BRC-4** as the consumption of oxygen and the increase of text temperature, which is in accordance with the ESR results. XPS spectra are also carried out to investigate the surface chemical composition of the as-prepared **BRC** samples, as depicted in Fig. S6 (Supporting Information). In the high resolution O 1s XPS spectra of **BRC** samples (Fig. 4c), it is found that an obvious peak shoulder located at 533.7 and 531.8 eV in **BRC-1** and **BRC-3**, which corresponds to

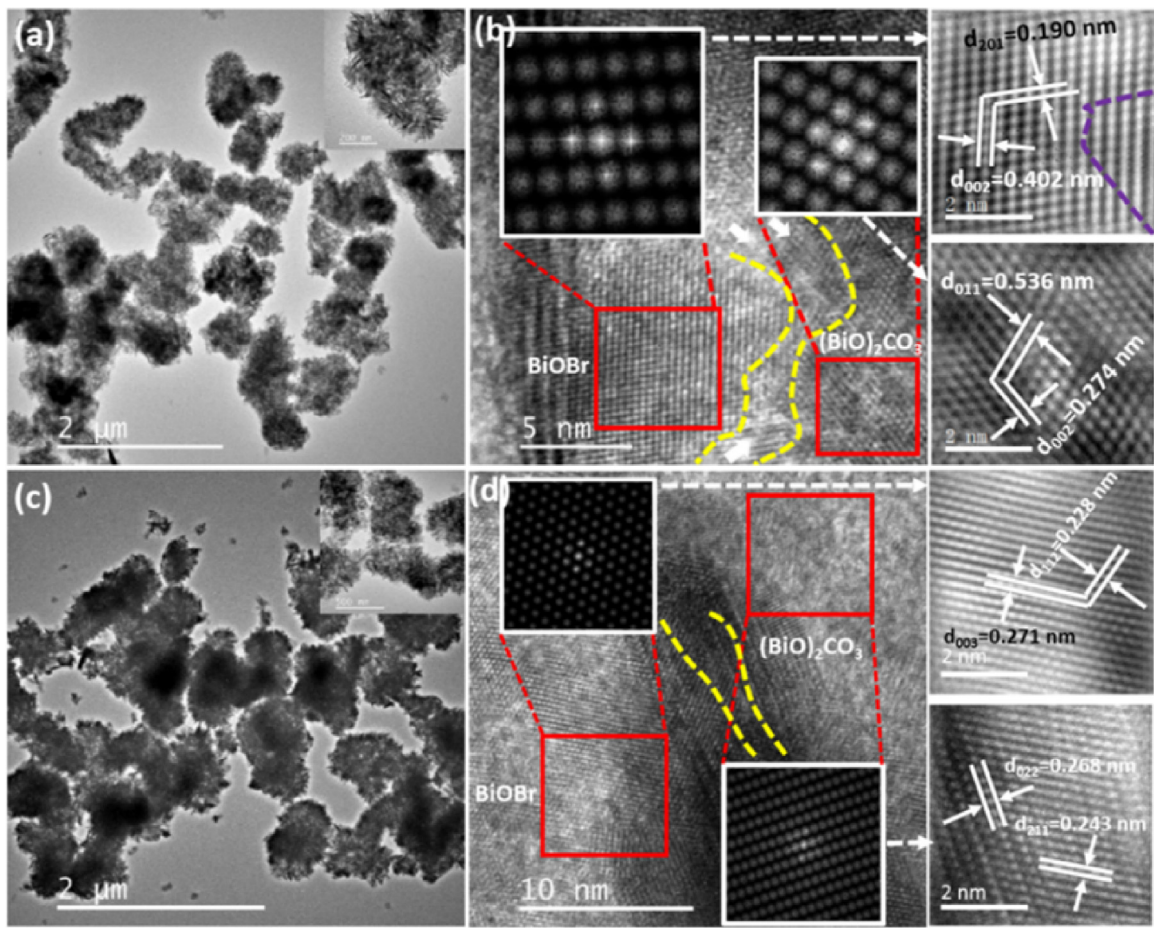


Fig. 5. TEM, HRTEM and the corresponding IFFT images of **BRC-1** (a and b), **BRC-2** (c and d).

the oxygen deficient regions (ODR) and normal oxygen region in the crystal structure, respectively [27,30]. The slightly peak shift of O 1s binding energy in **BRC-1** and **BRC-3** is probably due to the variation of the chemical coordination of O^{2-} in the two samples. However, only one peak which belongs to normal O in the crystal structure is observed in the O 1s spectra of **BRC-2** and **BRC-4** these two samples. Meanwhile, the binding energies of **BRC-2** and **BRC-4** also present slight difference, which is attribute to the variation of chemical environment of BiOBr and BiOBr/ $\text{Bi}_2\text{O}_2\text{CO}_3$ heterojunction [31]. Fig. 4d presents the high resolution Bi 4f XPS spectra of **BRC** samples. Compared with **BRC-2**, the characteristic peaks of Bi 4f_{5/2} and Bi 4f_{7/2} in the spectra of **BRC-1** shift to low binding energy. Similar result is also found in the XPS spectra of **BRC-3** and **BRC-4**. It might be attributed to the chemical coordination variation of Bi³⁺ in the absence and presence of oxygen vacancies. [32–35]

Fig. 5 shows the corresponding TEM images of **BRC-1** and **BRC-2**, which demonstrates similar hierarchical aggregated plate-like or sheet-like nanostructures, (Fig. 5a and c). HRTEM images further reveal the insight information of the heterojunction structure of **BRC-1** and **BRC-2**, as depicted in Fig. 5b and d. Fast Fourier Transform (FFT) images of the selected area demonstrate two sets of typical crystallographic symmetry of lattice dots which belongs to BiOBr and $\text{Bi}_2\text{O}_2\text{CO}_3$, respectively (Inset of Fig. 5b and d). Two sets of distinct lattice fringes are observed in the Inverse Discrete Fourier Transform (IFFT) of HRTEM images of both **BRC-1** and **BRC-2**, which comes from two different crystal phases and corresponds to d-spacing of cubic phase BiOBr and orthorhombic $\text{Bi}_2\text{O}_2\text{CO}_3$, respectively (Inset of Fig. 5b and d). However, the interface of BiOBr and $\text{Bi}_2\text{O}_2\text{CO}_3$ in **BRC-1** sample presents evident crystal dis-

order, which might be attributed to oxygen vacancies existed in **BRC-1** samples [27,36]. Therefore, **BRC-1** could be presented as $\text{BiO}_{1-x}\text{Br}/\text{Bi}_2\text{O}_2\text{CO}_3$ due to the existence of oxygen vacancy.

3.4. Reactive oxygen species (ROS) determination

The presence of oxygen vacancy in $\text{BiO}_{1-x}\text{Br}/\text{Bi}_2\text{O}_2\text{CO}_3$ heterostructure has a significant influence on the reactive oxygen species (ROS) production. Hence, ESR-DMPO method is used to determine the produced ROS in photocatalysis. As shown in Fig. 6a, in the presence of DMPO, obvious superoxide radical anions ($\bullet\text{O}_2^-$) signal is observed in the ESR spectrum of $\text{BiO}_{1-x}\text{Br}/\text{Bi}_2\text{O}_2\text{CO}_3$ (**BRC-1**) sample. No DMPO- $\bullet\text{O}_2^-$ signal is detected in the ESR spectrum of **BRC-2** sample. Similarly, DMPO- $\bullet\text{OH}$ signal only could be detected in the ESR spectrum of **BRC-1** sample, as demonstrated in Fig. 6b. It illustrates that $\bullet\text{O}_2^-$ and $\bullet\text{OH}$ radicals are only generated in $\text{BiO}_{1-x}\text{Br}/\text{Bi}_2\text{O}_2\text{CO}_3$ (**BRC-1**) sample. To further confirm the production of $\bullet\text{O}_2^-$ in **BRC-1**, nitrobluetetrazolium (NBT) is used as $\bullet\text{O}_2^-$ scavenger to capture generated $\bullet\text{O}_2^-$. It was observed that the content of NBT gradually decreased with the increase of irradiation time over **BRC-1**, while the amount of NBT keeps unchanged with prolonging irradiation over **BRC-2** (Fig. 6c). Meanwhile, the relative concentration of $\bullet\text{OH}$ was estimated by a TA-NaOH fluorescence method, as depicted in Fig. 6d. The peak intensity at 425 nm of **BRC-1** is much stronger than that of **BRC-2**, further verifying the production of $\bullet\text{OH}$ over **BRC-1** in the photocatalysis. The results illustrate that the oxygen vacancy in $\text{BiO}_{1-x}\text{Br}/\text{Bi}_2\text{O}_2\text{CO}_3$ (**BRC-1**) could promote the production of $\bullet\text{OH}$ and $\bullet\text{O}_2^-$. In order to understand the function of ROS in CIP photodegradation, t-

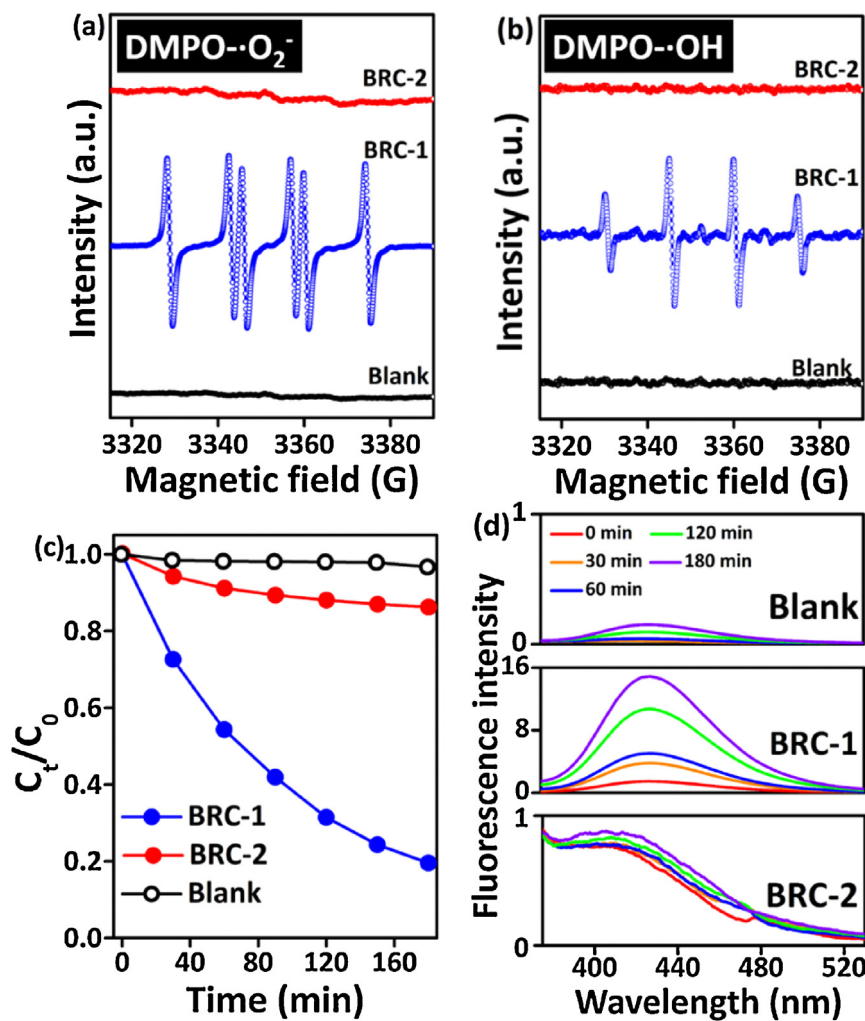


Fig. 6. ESR spectra of DMPO-•O₂⁻ (a), DMPO-•OH (b), dynamic conversion of NBT (c) and TA-NaOH fluorescence spectra (d) in the presence of **BRC-1** and **BRC-2** under visible light irradiation.

BuOH and N₂ were employed as •OH and •O₂⁻ scavengers in the photodegradation of CIP, respectively. As shown in Fig. S7 (Supporting Information), the photocatalytic degradation efficiency of CIP over BiO_{1-x}Br/Bi₂O₂CO₃ (**BRC-1**) significantly decrease in the presence of N₂ or t-BuOH, indicating that •O₂⁻ and •OH has significant influence on the degradation of CIP. However, no obvious changes in photodegradation efficiency over BiOBr/Bi₂O₂CO₃ (**BRC-2**) is observed in the presence of N₂ and t-BuOH, due to the absence of •O₂⁻ and •OH.

3.5. Photocatalytic mechanism of Z-scheme BiO_{1-x}Br/Bi₂O₂CO₃

To investigate the mechanism of the improved photocatalytic activity of BiO_{1-x}Br/Bi₂O₂CO₃, UV-vis diffuse reflection spectra (DRS) are acquired to determine the band structure of the samples. Fig. 7a displays the DRS spectra of the as-prepared **BRC** samples (**BRC-1**, **BRC-3** and **BRC-5**). The corresponding band gap can be calculated by the Kubelka–Munk (KM) expression [37,38]:

$$\alpha h\nu = A(h\nu - E_g)^{n/2} \quad (2)$$

where A, $h\nu$, E_g , and α are the proportionality constant, photonic energy, band gap, and optical absorption coefficient, respectively. The calculated band gaps of **BRC-1**, **BRC-3**, and **BRC-5** are 2.60, 2.25, and 2.87 eV, respectively (inset of Fig. 7a). Based on Mott-Schottky plots of **BRC-3** and **BRC-5** (Fig. 7b), the calculated flat band potential

(V_{fb}) of **BRC-3** and **BRC-5** are −0.48 and −0.08 eV vs. NHE, respectively. Accordingly, the valence band potential (E_{VB}) of **BRC-3** and **BRC-5** are 1.77 and 2.79 eV, respectively, based on the empirical formula ($Eg = E_{VB} - E_{CB}$). Band XPS spectra (inset in Fig. 7b) are also used to confirm the band structure, and the band potentials (1.75 eV for **BRC-3** and 2.77 eV for **BRC-5**) are consistent with the calculated results from Mott-Schottky plots.

Generally, the composited BiOBr/Bi₂O₂CO₃ photocatalytic system should be expressed as a heterojunction type photocatalyst, as illustrated in Scheme 1a. [39,40]. Due to the potential difference, the excited electrons transfer from the CB of BiOBr to the CB of Bi₂O₂CO₃, resulting in the decrease of electron reducibility. Meanwhile, the photogenerated holes transfer from the VB of Bi₂O₂CO₃ to the VB of BiOBr, also leading to the decrease of hole oxidizability. Based on the calculated VB of BiOBr and CB of Bi₂O₂CO₃ in this photocatalytic system, •O₂⁻ and •OH radicals could not be produced due to the low electron reducibility and hole oxidizability. Therefore, it is proposed that a direct Z-scheme photocatalytic system is fabricated, as shown in Scheme 1b [16,41]. Upon simultaneous light excitation, both BiO_{1-x}Br and Bi₂O₂CO₃ phases could generate excited electron-hole pairs. The excited electrons from the CB of Bi₂O₂CO₃ can transfer to combine with the photogenerated holes in BiO_{1-x}Br via the oxygen vacancy, which acts as an electron mediator, thus preserving the strong reducibility of electron in the CB of BiO_{1-x}Br and the strong oxidizability of holes in the VB of

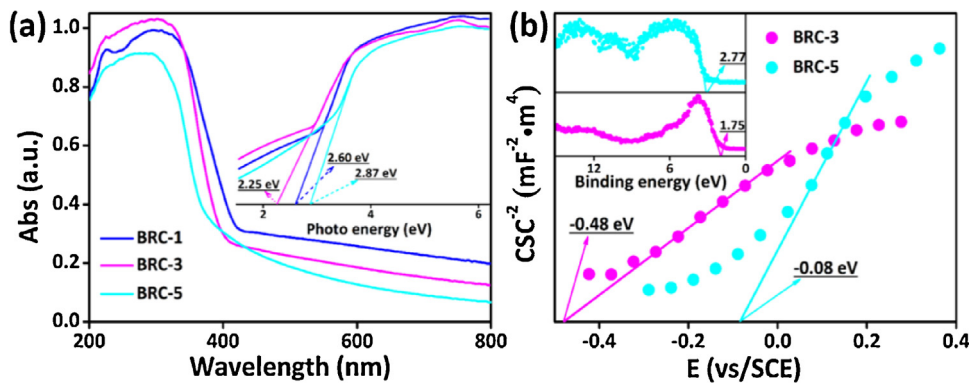
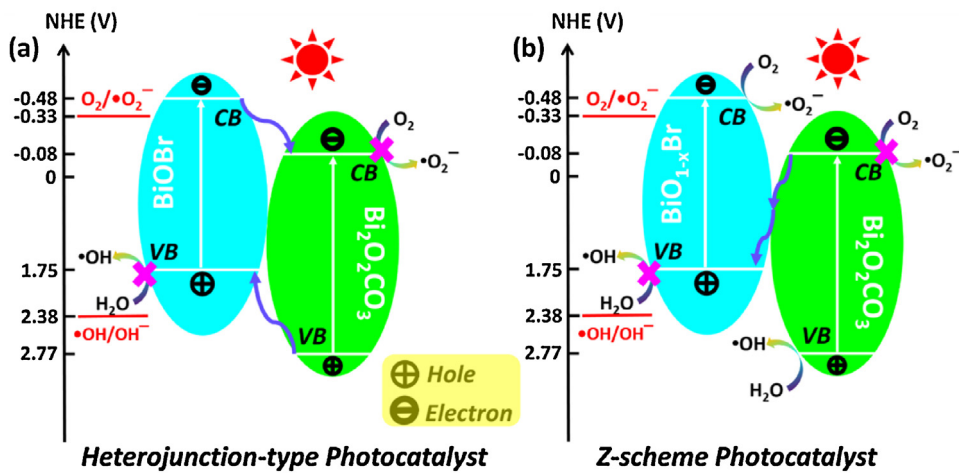


Fig. 7. UV-vis diffuse reflectance spectra and the plots of transformed Kubelka-Munk function versus light energy (inset) over **BRC-1**, **BRC-3**, and **BRC-5** (a), Mott-Schottky plots and band XPS spectra (inset) (b) of **BRC-3**, and **BRC-5**.



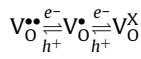
Scheme 1. Schematic illustration of two different photocatalytic systems: (a) heterojunction-type and (b) Z-scheme mechanisms photocatalytic system.

Bi₂O₂CO₃. As a result, •O₂^{·-} and •OH radicals could be produced in the photocatalytic reaction.

To further verify the formation of Z-scheme BrO_{1-x}Br/Bi₂O₂CO₃, the cyclic voltammetry (CV) and transient photocurrent responses of BiO_{1-x}Br/Bi₂O₂CO₃ (**BRC-1**) and BiOBr/Bi₂O₂CO₃ (**BRC-2**) are recorded by using electrochemical workstation. Fig. 8a shows that **BRC-1** has higher oxidation and reduction potential than that of **BRC-2**, indicative of strong oxidizability and reducibility [42]. Fig. 8b shows the photocurrent response of **BRC-1** and **BRC-2** electrodes under visible light illumination. It is found that photocurrent generated by **BRC-2** was significantly higher than that of **BRC-1** sample, suggesting that more photogenerated electrons are generated in BiOBr/Bi₂O₂CO₃ under visible light irradiation [37]. It is proposed that the present of oxygen vacancies could change the flow direction of electron, thus leading to stronger redox potential for BiO_{1-x}Br/Bi₂O₂CO₃, which is accord with electron migration path of Z-scheme photocatalytic system. In addition, electrochemical impedance spectroscopy (EIS) is employed to monitor the charge migration process. Fig. 8c shows the EIS Nyquist plots of the as-prepared samples. Compared with **BRC-2**, **BRC-1** presents the smaller arc radius of the EIS Nyquist plot, indicative of the fastest interfacial charge transference characteristics. It illustrates that **BRC-1** has positive effect on the separation and transfer efficiency of photogenerated electron-hole pairs. Photoluminescence (PL) is also performed to confirm the enhanced separation efficiency of photogenerated charge carriers. As shown in Fig. 8d, **BRC-1** sample displays weaker PL emission intensity than that of **BRC-2**, which is

probably due to the indirect recombination of photoinduced electrons and holes in **BRC-1**. It indicates that BiO_{1-x}Br/Bi₂O₂CO₃ could effectively enhance the separation efficiency of electron-hole pairs, thus resulting in improved photocatalytic performance.

To further understand the behavior of charge transfer, the PL spectra are resolved into several subemission bands (Fig. 9). As shown in Fig. 9a, ten emission bands (R1 ~ R10) are obtained by means of PL-peak-differentiation analysis for BiO_{1-x}Br/Bi₂O₂CO₃ (**BRC-1**). The near-UV emission (R1, 432 nm) is associated with the band-edge emission of Bi₂O₂CO₃, and the corresponding optical bandgap is approximately 2.87 eV [43]. The visible emission (R8, 563 nm) is associated with the band-edge emission of BiOBr, and the corresponding optical bandgap of which is approximately 2.20 eV. The other long-wavelength emission bands (450–650 nm) are attributed to defect emissions [44–49]. Among these emission bands, green emission bands (500–650 nm) are often assigned to the emission from ionized oxygen vacancies (V_O[·], V_O^{··}) and neutral oxygen vacancies (V_O[×]) located at the surface [46,47]. However, BiOBr/Bi₂O₂CO₃ (**BRC-2**) only exhibit four emission bands (P1–P4) (Fig. 9b), which belongs to intrinsic absorption of BiOBr and Bi₂O₂CO₃, respectively. Therefore, it is speculated that the trapping/detrapping of the electron from CB of Bi₂O₂CO₃ and holes from VB of BiO_{1-x}Br predominantly occur at the oxygen vacancy sites in the BiO_{1-x}Br/Bi₂O₂CO₃ photocatalytic [44,46,47].



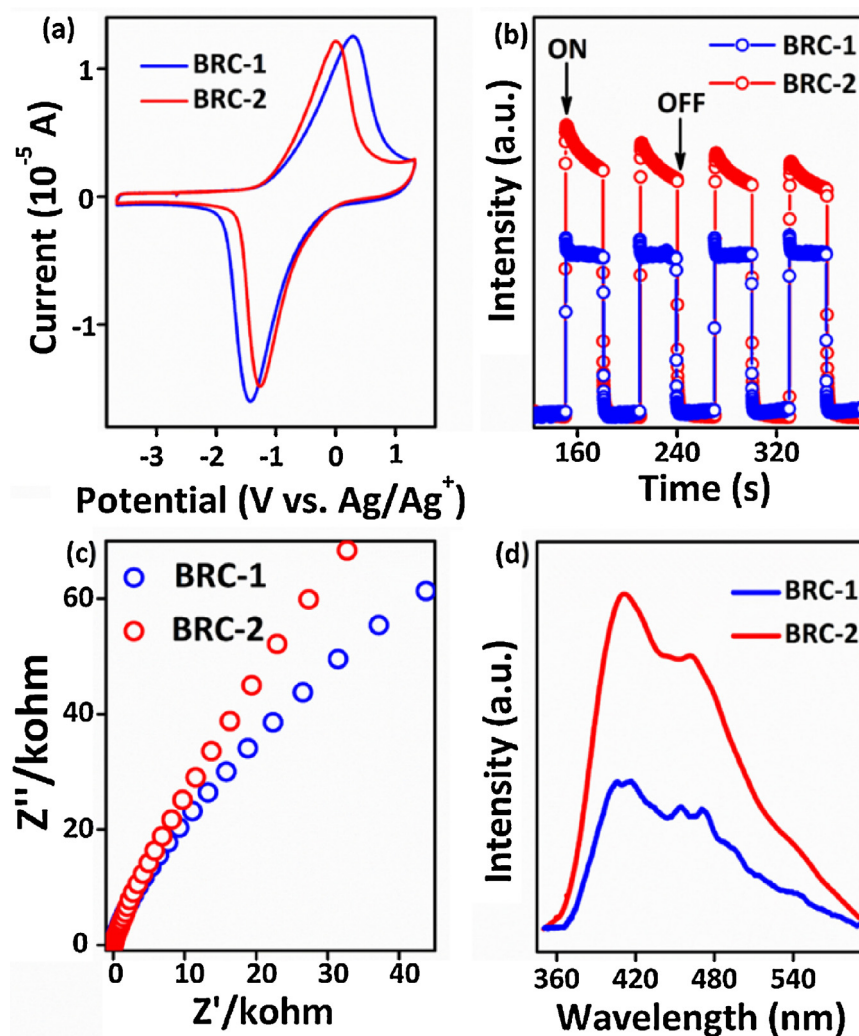


Fig. 8. CV curve (a, vs. Ag/Ag⁺ reference electrode), transient photocurrent densities (b), EIS Nyquist plots (c) and PL spectra (d) in the presence of the as-prepared BRC-1, BRC-2 samples.

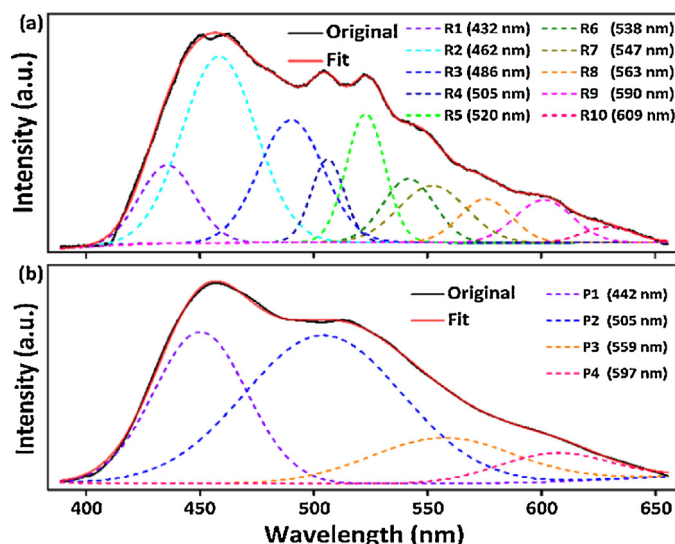


Fig. 9. Sub-band resolved room temperature photoluminescence (PL) emission spectra of BRC-1 (a) and BRC-2 (b).

This trapping/detrapping could mediate the electron and hole transfer and enhance charge separation efficiency. It further con-

firms that oxygen vacancy acts as electron mediator in Z-scheme BiO_{1-x}Br/Bi₂O₂CO₃ photocatalysis.

Based on above analysis, a detailed photocatalytic mechanism and the role of oxygen vacancies in the Z-scheme BiO_{1-x}Br/Bi₂O₂CO₃ system are proposed and illustrated in Scheme 2. In this photocatalytic system, photogenerated electrons on CB of BiO_{1-x}Br could react with O₂ to produce •O₂⁻ and holes on VB of Bi₂O₂CO₃ could involve in the production of •OH from H₂O. Ultimately, the produced ROS results in the mineralization of antibiotics to H₂O and CO₂. Oxygen vacancy acts as the electron mediator in the Z-scheme Bi_{1-x}Br/Bi₂O₂CO₃ system, also functioning as recombination or storage center of photogenerated charge carriers. It realizes the high separation efficiency of charge carriers, broad photoresponse range and strong redox ability of the BiO_{1-x}Br/Bi₂O₂CO₃ photocatalyst.

3.6. Photocatalytic degradation for antibiotics and organic pollutants

In addition, the strong redox ability of Z-scheme BiO_{1-x}Br/Bi₂O₂CO₃ photocatalyst is also demonstrated by the degradation of BPA and 4-MAA. As shown in Fig. 10, the photodegradation efficiency of BPA and 4-MAA over BRC-1 is much higher than that of BRC-2 sample. The apparent rate constant per unit surface area of BRC-1 (k/S_{BET} , $13.24 \times 10^{-3} \text{ m}^{-2} \text{ h}^{-1}$ for BPA and

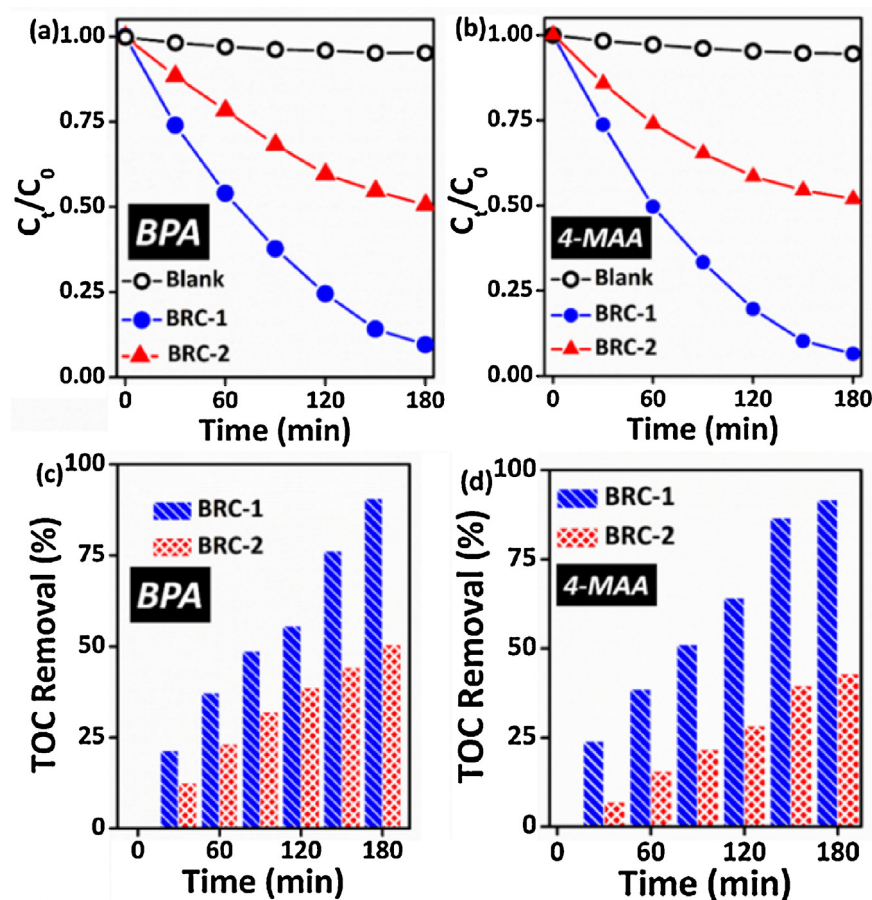
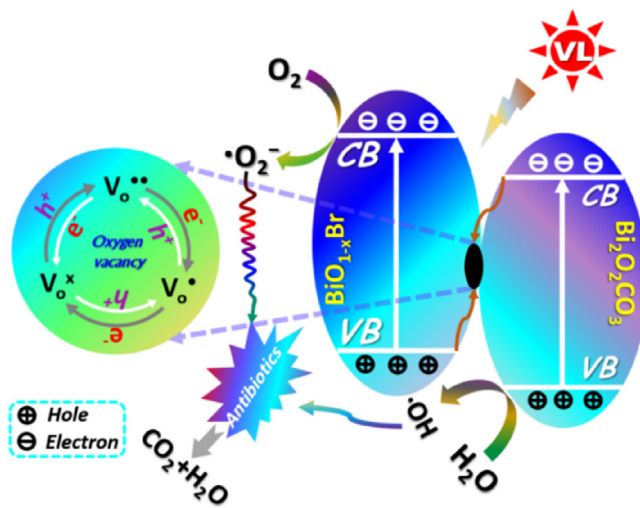


Fig. 10. Photodegradation efficiencies of BPA (a) and 4-MAA (b), TOC removal efficiencies of BPA (c) and 4-MAA (d) over **BR-C-1** and **BR-C-2** under visible light irradiation, respectively.



Scheme 2. Illustration of photocatalytic mechanisms of Z-scheme $\text{BiO}_{1-x}\text{Br}/\text{Bi}_2\text{O}_2\text{CO}_3$.

$15.53 \times 10^{-3} \text{ m}^{-2} \text{ h}^{-1}$ for 4-MAA) are also much higher than that of **BR-C-2** ($4.10 \times 10^{-3} \text{ m}^{-2} \text{ h}^{-1}$ for BPA and $2.35 \times 10^{-3} \text{ m}^{-2} \text{ h}^{-1}$ for 4-MAA), as shown in Fig. S8 (Supporting Information). More importantly, the mineralization of BPA and 4-MAA over **BR-C-1** and **BR-C-2** photodegradation is also investigated by TOC removal measurement (Fig. 10c and 10d). Only $\text{BiO}_{1-x}\text{Br}/\text{Bi}_2\text{O}_2\text{CO}_3$ could degrade BPA and 4-MAA completely. However, more than 50% of total organic carbon still remained in BPA and 4-MAA solution of

BR-C-2, indicative of low mineralization. The complete mineralization and photodegradation pathway of BPA and 4-MAA over **BR-C-1** is further verified by HPLC-MS analysis (Fig. S9 and S10, Supporting Information). The corresponding HPLC-MS analysis also reveals the incomplete degradation of BPA and 4-MAA over **BR-C-2** under identical conditions (Fig. S11 and S12, Supporting Information). Moreover, Z-schemed $\text{BiO}_{1-x}\text{Br}/\text{Bi}_2\text{O}_2\text{CO}_3$ photocatalyst still remains high photocatalytic activity after four recycles (Fig. S13, Supporting Information).

4. Conclusion

In summary, a Z-scheme $\text{BiO}_{1-x}\text{Br}/\text{Bi}_2\text{O}_2\text{CO}_3$ photocatalyst has been successfully synthesized via a facile solvothermal method by varying reaction time. The $\text{BiO}_{1-x}\text{Br}/\text{Bi}_2\text{O}_2\text{CO}_3$ nanocomposite with rich oxygen vacancy exhibits highly enhanced performance for the photodegradation of antibiotics (CIP, 4-MAA) and other organic pollutants, compared with non-oxygen vacancy involved $\text{BiOBr}/\text{Bi}_2\text{O}_2\text{CO}_3$ photocatalyst, single-component $\text{BiO}_{1-x}\text{Br}$ and $\text{Bi}_2\text{O}_2\text{CO}_3$. Only $\text{BiO}_{1-x}\text{Br}/\text{Bi}_2\text{O}_2\text{CO}_3$ photocatalyst could degrade the tested antibiotics completely, as confirmed by HPLC-MS and TOC removal analysis. By photoluminescence and photoelectrochemical measurement, it is found that oxygen vacancy serves as the electron mediator to promote the enhancement of redox ability and the production of ROS (O_2^\cdot and OH^\cdot) for the photodegradation of antibiotics. This work provides a novel strategy to construct Z-scheme photocatalytic system via oxygen vacancy as electron mediator for interfacial charges migration, thus promoting the photocatalytic efficiency. It also demonstrates the superior photo-

catalytic efficiency of Z-scheme $\text{BiO}_{1-x}\text{Br}/\text{Bi}_2\text{O}_2\text{CO}_3$ nanocomposite for complete degradation of antibiotics, due to its high separation efficiency of charge carriers, strong redox ability and broad photoresponse range.

Acknowledgements

This work was supported by the National Natural Science Foundation of China (21471121 and 21671153), Department of Education of Hubei Province under the project of Science and Technology Innovation Team of Outstanding Young and Middle-aged Scientists (T201606) and High-Tech Industry Technology Innovation Team Training Program of Wuhan Science and Technology Bureau (2014070504020243).

Appendix A. Supplementary data

Supplementary data associated with this article can be found, in the online version, at <http://dx.doi.org/10.1016/j.apcatb.2016.12.018>.

References

- [1] Y.G. Zhu, T.A. Johnson, J.Q. Su, M. Qiao, G.X. Guo, R.D. Stedtfeld, S.A. Hashsham, J.M. Tiedje, Proc. Natl. Acad. Sci. 110 (2013) 3435–3440.
- [2] Q.Q. Zhang, G.G. Ying, C.G. Pan, Y.S. Liu, J.L. Zhao, Environ. Sci. Technol. 49 (2015) 6772–6782.
- [3] G.D. Wright, Curr. Opin. Microbiol. 13 (2010) 589–594.
- [4] W. Witte, Science 279 (1998) 996–997.
- [5] T. Paul, P.L. Miller, T.J. Strathmann, Environ. Sci. Technol. 41 (2007) 4720–4727.
- [6] D. Li, S. Zeng, M. He, A.Z. Gu, Environ. Sci. Technol. 50 (2016) 3193–3201.
- [7] J.M. Elward, A. Chakraborty, J. Chem. Theory Comput. 9 (2013) 4351–4359.
- [8] W.K. Jo, T.S. Natarajan, ACS Appl. Mater. Interfaces 7 (2015) 17138–17154.
- [9] P. Zhou, J. Yu, M. Jaroniec, Adv. Mater. 26 (2014) 4920–4935.
- [10] A. Iwase, Y.H. Ng, Y. Ishiguro, A. Kudo, R. Amal, J. Am. Chem. Soc. 133 (2011) 11054–11057.
- [11] M.G. Ahmed, T.A. Kandiel, A.Y. Ahmed, I. Kretschmer, F. Rashwan, D. Bahnemann, J. Phys. Chem. C 119 (2015) 5864–5871.
- [12] F. Dong, Z. Zhao, T. Xiong, Z. Ni, W. Zhang, Y. Sun, W.K. Ho, ACS Appl. Mater. Interfaces 5 (2013) 11392–11401.
- [13] B. Liu, A. Khare, E.S. Aydil, ACS Appl. Mater. Interfaces 3 (2011) 4444–4450.
- [14] X. Wang, S. Blechert, M. Antonietti, ACS Catal. 2 (2012) 1596–1606.
- [15] Q. Jia, A. Iwase, A. Kudo, Chem. Sci. 5 (2014) 1513.
- [16] K. Maeda, D. Lu, K. Domen, ACS Catal. 3 (2013) 1026–1033.
- [17] Y. Sasaki, A. Iwase, H. Kato, A. Kudo, J. Catal. 259 (2008) 133–137.
- [18] P. Yang, J. Zhao, J. Wang, B. Cao, L. Li, Z. Zhu, J. Mater. Chem. A 2 (2015) 8256–8259.
- [19] L.J. Zhang, S. Li, B.K. Liu, D.J. Wang, T.F. Xie, ACS Catal. 4 (2014) 3724–3729.
- [20] M. Miyauchi, Y. Nukui, D. Atarashi, E. Sakai, ACS Appl. Mater. Interfaces 5 (2013) 9770–9776.
- [21] N. Srinivasan, E. Sakai, M. Miyauchi, ACS Catal. 6 (2016) 2197–2200.
- [22] Z. Dai, F. Qin, H. Zhao, F. Tian, Y. Liu, R. Chen, Nanoscale 7 (2015) 11991–11999.
- [23] F. Tian, H. Zhao, G. Li, Z. Dai, Y. Liu, R. Chen, ChemSusChem 9 (2016) 1579–1585.
- [24] Z. Dai, F. Qin, H. Zhao, J. Ding, Y. Liu, R. Chen, ACS Catal. 6 (2016) 3180–3192.
- [25] P. Calza, C. Medana, F. Carbone, V. Giancotti, C. Baiocchi, Rapid. Commun. Mass. Spectrom. 22 (2008) 1533–1552.
- [26] X. Zhang, R. Li, M. Jia, S. Wang, Y. Huang, C. Chen, Chem. Eng. J. 274 (2015) 290–297.
- [27] X. Pan, M.Q. Yang, X. Fu, N. Zhang, Y.J. Xu, Nanoscale 5 (2013) 3601–3614.
- [28] M.H. Jang, R. Agarwal, P. Nukala, D. Choi, A.T. Johnson, I.W. Chen, R. Agarwal, Nano Lett. 16 (2016) 2139–2144.
- [29] B. Bonnetot, R.T. Yuzhakova, C. Guimon, A. Auroux, Chem. Mater. 20 (2008) 1158–1159.
- [30] X. Xiong, L. Ding, Q. Wang, Y. Li, Q. Jiang, J. Hu, Appl. Catal. B 188 (2016) 283–291.
- [31] B. Santara, P.K. Giri, K. Imakita, M. Fujii, Nanoscale 5 (2013) 5476–5488.
- [32] Y. Lv, Y. Liu, Y. Zhu, Y. Zhu, J. Mater. Chem. A 2 (2014) 1174–1182.
- [33] Z.P. Nie, D.K. Ma, G.Y. Fang, W. Chena, S.M. Huang, J. Mater. Chem. A 4 (2016) 2438–2444.
- [34] Y. Huang, H. Li, M.S. Balogun, W. Liu, Y. Tong, X. Lu, H. Ji, ACS Appl. Mater. Interfaces 6 (2014) 22920–22927.
- [35] L. Zhang, W. Wang, D. Jiang, E. Gao, S. Sun, Nano Res. 8 (2014) 821–831.
- [36] X. Chen, L. Liu, P.Y. Yu, S.S. Mao, Science 331 (2011) 746–750.
- [37] F. Tian, Y. Zhang, G. Li, Y. Liu, R. Chen, New J. Chem. 39 (2015) 1274–1280.
- [38] H. Zhao, Y. Zhang, G. Li, F. Tian, H. Tang, R. Chen, RSC Adv. 6 (2016) 7772–7779.
- [39] C. Liu, H. Huang, X. Du, T. Zhang, N. Tian, Y. Guo, Y. Zhang, J. Phys. Chem. C 119 (2015) 17156–17165.
- [40] W.Y. Teoh, J.A. Scott, R. Amal, J. Phys. Chem. Lett. 3 (2012) 629–639.
- [41] L. Ye, J. Liu, C. Gong, L. Tian, T. Peng, L. Zan, ACS Catal. 2 (2012) 1677–1683.
- [42] Y. Myung, F. Wu, S. Banerjee, J. Park, P. Banerjee, Chem. Commun. 51 (2015) 2629–2632.
- [43] T. Zhao, J. Zai, M. Xu, Q. Zou, Y. Su, K. Wang, X. Qian, CrystEngComm 13 (2011) 4010–4017.
- [44] A.B. Djurisic, Y.H. Leung, Small 2 (2006) 944–961.
- [45] M. Guan, C. Xiao, J. Zhang, S. Fan, R. An, Q. Cheng, J. Xie, M. Zhou, B. Ye, Y. Xie, J. Am. Chem. Soc. 135 (2013) 10411–10417.
- [46] H.W. Jeong, S.Y. Choi, S.H. Hong, S.K. Lim, D.S. Han, A.A. Wahab, H. Park, J. Phys. Chem. C 118 (2014) 21331–21338.
- [47] S.K. Lim, S.H. Hwang, S. Kim, H. Park, Sens. Actuators B 160 (2011) 94–98.
- [48] J. Pal, A.K. Sasmal, M. Ganguly, T. Pal, J. Phys. Chem. C 119 (2015) 3780–3790.
- [49] G. Xi, J. Ye, Inorg. Chem. 49 (2010) 2302–2309.